

# A Power-Frequency Controller With Resonance Frequency Tracking Capability for Inductive Power Transfer Systems

Masood Moghaddami<sup>1</sup>, Student Member, IEEE, Aditya Sundararajan<sup>2</sup>, Student Member, IEEE, and Arif I. Sarwat<sup>3</sup>, Senior Member, IEEE

**Abstract**—A self-tuning controller for power transfer regulation in inductive power transfer (IPT) systems is proposed in this paper. The controller enables power transfer regulation around a user-defined reference power level. The converter's efficiency is improved by constantly tuning the switching operations to the resonant current, thereby achieving the soft-switching operations reducing electromagnetic interference in the power converters. The self-tuning capability makes it ideal for dynamic IPT systems with uncertain loads and fluctuating resonance frequency. High operating frequencies can be achieved using the simplified digital circuit design for the controller, proposed in this paper, which delivers a low total propagation delay. Bidirectional power transfer can be enabled by using the proposed controller on both transmitter and receiver sides. In the reverse power flow mode, the primary converter operates as a rectifier and the power transfer is controlled through the secondary converter using the proposed controller. The performance of the proposed controller is analyzed using MATLAB/Simulink and the results are presented. Finally, the proposed controller is implemented experimentally and its performance is evaluated as a case study on an IPT system. The experimental and simulation results conform to each other, and show that the proposed converter can effectively regulate the power transfer with an improved efficiency.

**Index Terms**—Inductive power transfer (IPT), power control, self-tuning control, soft switching.

## I. INTRODUCTION

INDUCTIVE power transfer (IPT) systems based on the resonant magnetic induction constitute a new technology that enables power transmission between two systems without physical contacts. Owing to its superior robustness, reliability, and safety in comparison with the existing methods, they are applied widely as biomedical implants [1], material handling [2],

Manuscript received February 15, 2017; revised May 6, 2017, July 18, 2017, and September 26, 2017; accepted November 6, 2017. Date of publication December 3, 2017; date of current version March 19, 2018. Paper 2017-IACC-0045.R3, presented at the 2016 IEEE International Conference on Power Electronics, Drives, and Energy Systems, Trivandrum, India, Dec. 14–17, and approved for publication in the IEEE TRANSACTIONS ON INDUSTRY APPLICATIONS by the Industrial Automation and Control Committee of the IEEE Industry Applications Society. This work was supported by the National Science Foundation under Grant 1553494. (Corresponding author: Arif I. Sarwat.)

The authors are with the Department of Electrical and Computer Engineering, Florida International University, Miami FL 33174 USA (e-mail: mmogh003@fiu.edu; asund005@fiu.edu; asarwat@fiu.edu).

Color versions of one or more of the figures in this paper are available online at <http://ieeexplore.ieee.org>.

Digital Object Identifier 10.1109/TIA.2017.2779425

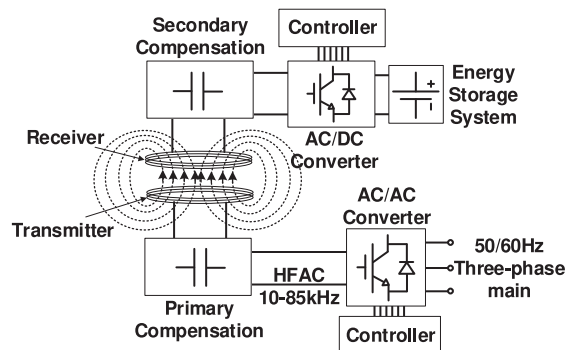


Fig. 1. Typical structure of an IPT system.

and transportation systems [3]. Over the recent years, the IPT-based charging systems for contactless electric vehicles (EVs) has been on the rise, broadly categorized as static [4], [5] and dynamic or in-motion charging modes [6], [7].

Presenting themselves as a formidable alternative to the traditional wired charging in EV charging stations, static EV charging systems provide more safety and convenience to the users of EVs. At the same time, a growing interest has emerged in the dynamic EV charging systems, and it is now regarded as one of the technological cornerstones that can revolutionize the world of transportation systems. The contactless EV charging systems are equipped with bidirectional power flow capabilities to enable grid-to-vehicle and vehicle-to-grid (V2G) connections [8]. Improving the resiliency of the future infrastructure of smart grid is touted to be one of the major benefits of V2G connections, since they can afford to support the grid under extreme conditions, or through peak shaving [9], [10]. The structure of a typical IPT system is illustrated in Fig. 1.

Power flow control plays a crucial role in the IPT system's optimal operation, which can, in turn, be attained by controlling the transferred power to either the transmitter or the receiver, or both [11]. In the literature, several techniques for power flow control for IPT systems exist, including resonance frequency control [12], power-frequency control [13]–[15], phase-shift control [16]–[18], load detection [19], reactive power control [11], and sliding-mode control [20], [21]. Tuning the control parameters and handling the system variability can be made possible by modifying the control methods to be adaptive with

TABLE I  
DISTINCT POWER TRANSFER LEVELS AND CORRESPONDING  
ENERGY-INJECTION FREQUENCIES FOR POSITIVE  
AND NEGATIVE HALF-CYCLES

| Power Level $n-m$ | Frequency of Energy Injection       |                                     |
|-------------------|-------------------------------------|-------------------------------------|
|                   | Positive Half-Cycles<br>( $f_r/n$ ) | Negative Half-Cycles<br>( $f_r/m$ ) |
| Level 1-1         | $f_r$                               | $f_r$                               |
| Level 1-2         | $f_r$                               | $f_r/2$                             |
| Level 1-4         | $f_r$                               | $f_r/4$                             |
| Level 1-8         | $f_r$                               | $f_r/8$                             |
| Level 2-2         | $f_r/2$                             | $f_r/2$                             |
| Level 2-4         | $f_r/2$                             | $f_r/4$                             |
| Level 2-8         | $f_r/2$                             | $f_r/8$                             |
| Level 4-4         | $f_r/4$                             | $f_r/4$                             |
| Level 4-8         | $f_r/4$                             | $f_r/8$                             |
| Level 8-8         | $f_r/8$                             | $f_r/8$                             |

self-tuning capability [22], [23]. The self-tuning capability of such controllers can significantly enhance the performance and interoperability of IPT systems.

Soft-switching operations in power converters can significantly improve the efficiency and reduce their electromagnetic field interference (EMI) [24]. Since IPT systems for EV applications usually operate at frequencies ranging between 20 and 85 kHz, the performance of the power converters considerably affect their performance. Thus, by ensuring soft-switching operations of the converter, the controllers can greatly improve the performance of the system. One method capable of effective power flow control in IPT systems is the energy-injection free-oscillation. This technique that enables soft-switching operations has been successfully applied in many studies [22], [25]–[27].

Conventionally, pulse-width modulation (PWM) based power electronic converters are used in IPT systems, and desired outputs are achieved by controlling the frequency and duty cycle of the PWM signal [28], [29]. In [22] and [30], a control method based on a variable frequency control technique is proposed for inductive EV charging systems, which is utilized in this paper. This method achieves multiple power transfer levels in a full-bridge dc/ac converter, and is designed to reduce the frequency of energy injection (rather than changing the duty cycle of a PWM signal) without compromising the resonance behavior of the IPT system. The developed controller is open loop and provides multiple power transfer levels. It is noteworthy that the terms “energy-injection level” and “power transfer level” mean the same and are, hence, used interchangeably throughout this paper.

The main contribution of this paper is the proposition, design, and implementation of a power-frequency controller that regulates the power transfer rate in accordance with the desired level (specified by the user) and tracks the resonance frequency of the system in a way that maximizes the power transfer efficiency. This controller also ensures its performance is not affected by system changes due to dynamic variations, as is the case in roadway IPT systems. Above all, the method proposed in this paper simplifies the design and complexity of the controller,

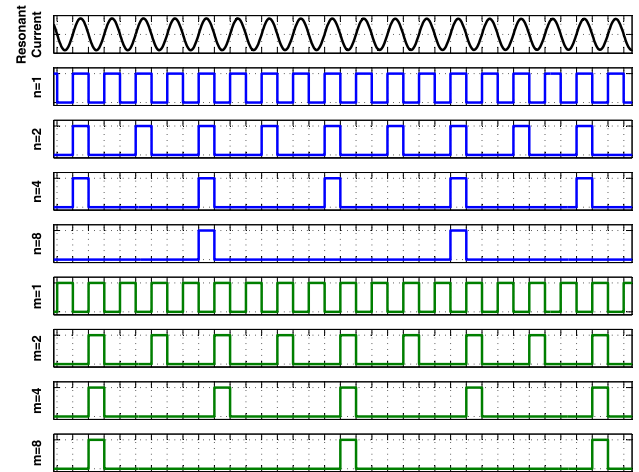


Fig. 2. Resonant current and corresponding positive and negative half-cycle energy-injection signals for  $n, m \in \{1, 2, 4, 8\}$ .

thereby reducing implementation costs. The existing methods in literature fall short in all of the above aspects, highlighting the uniqueness of the proposed controller. Although the proposed controller leverages similar benefits in terms of its self-tuning capability, low EMI, soft-switching operations, low switching stress, etc., its real novelty lies in the simplified, cost-effective design, and its ability to maximize power transfer efficiency even in dynamic system environments. A digital circuit based design and implementation of the proposed controller is presented, which is capable of effectively regulating the transferred power. In order to validate the controller’s efficacy, it is analyzed theoretically, simulated in MATLAB/Simulink, and then experimentally implemented, the results of which are discussed in detail.

## II. PROPOSED CONTROL METHOD

A control method based on the variable-frequency energy-injection and free-oscillation technique for IPT systems is presented in [22], which provides ten power transfer levels (see Table I). These power levels are achieved by independently controlling the frequency of energy injection into the IPT system at positive and negative half-cycles of the resonant current. The power transfer levels are labeled as  $n-m$ , where  $n$  and  $m$  correspond to  $f_r/n$  and  $f_r/m$  energy-injection frequencies for positive and negative half-cycles, respectively (where  $f_r$  is the resonance frequency). Fig. 2 conceptually shows the positive and negative half-cycle energy-injection signals for different power levels ( $n, m \in \{1, 2, 4, 8\}$ ). In this study, the control technique is further developed in order to design a closed-loop self-tuning controller that enables power transfer regulation in IPT systems. This is achieved by designing a control loop for power level that can regulate the power level around the reference power ( $P_{ref}$ ) by switching between energy-injection states presented in Table I.

### A. Power-Frequency Controller

The proposed controller along with a full-bridge dc/ac converter connected to an  $RLC$  is shown in Fig. 3. The  $RLC$  load

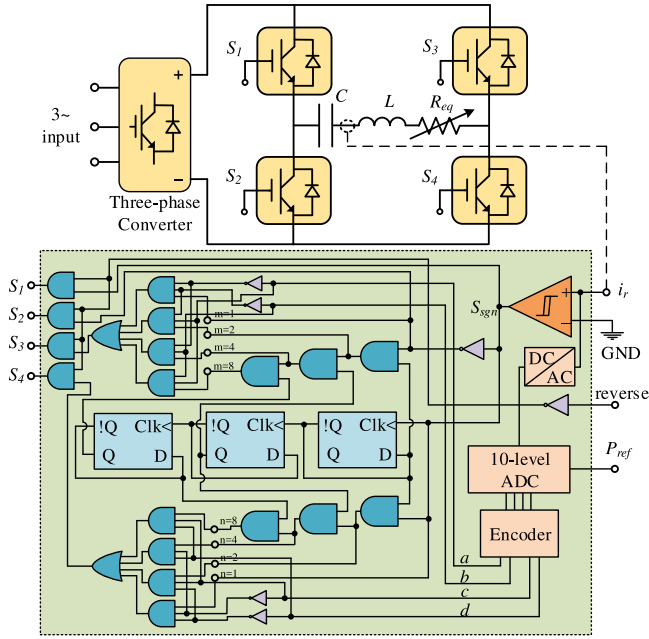


Fig. 3. Proposed power-frequency controller design based on a digital control circuit.

represents the IPT system where  $L$  is the self-inductance of the primary coil,  $C$  is the series compensation capacitor, and  $R_{eq}$  is the equivalent reflected resistance of the secondary. The controller takes the resonant current as feedback and generates four output signals to control the full-bridge converter based on the reference power level ( $P_{ref}$ ). The proposed controller is comprised of a differential comparator, AND, OR, NOT logic gates, flip-flops, signal rectifier, a ten-level analog-to-digital converter (ADC), and an encoder.

Fig. 2 conceptually shows the positive and negative half-cycle energy-injection signals for different power levels ( $n, m \in \{1, 2, 4, 8\}$ ), which are presented in Table I, and the control circuit diagram is shown in Fig. 3. These energy-injection signals are generated using a three-stage frequency divider (three flip-flops connected in series) and are routed to the output switching signals using two four-input multiplexer circuits (combination of two NOT gates, four AND gates, and an OR gate). The multiplexers are switched using four selectors ( $a$  and  $b$  for negative half-cycles, and  $c$  and  $d$  for positive half-cycles) that are determined based on the resonant current amplitude and the reference power ( $P_{ref}$ ).

The circuit is designed to achieve zero-current switching (ZCS) by synchronizing the switching operations with the resonant current. This is done using the output of the resonant current zero-cross detector (output of the differential comparator,  $S_{sgn}$ ) as a clock source signal for the resonance frequency divider. The frequency divider is used to change the energy-injection frequency in order to control the power transfer level. A signal rectifier (ac/dc converter) is used to convert the measured ac resonant current into a dc signal in order to enable comparisons with the reference level. This signal determines the level of the resonant current. Using an ADC, the corresponding dc signal is

then converted to a four-digit signal by comparing the equivalent dc signal to the reference level input. Based on the level of the resonant current, the encoder generates four signals to control the power transfer level and minimize the power level error with respect to the reference power level. The power transfer control is achieved by tuning the frequency of energy injection to the IPT systems using two multiplexer circuits for positive and negative half-cycle energy-injection signals, which are generated by the resonance frequency divider circuits (series-connected flip-flops and corresponding logic gates).

The “reverse” input is used to enable reverse power flow mode by disabling all the switching signals and, thus, allowing the converter to operate as a rectifier. In this case, the secondary coil works as a transmitter and the primary coil works as a receiver allowing a reverse power flow. If the primary circuit is powered by an ac source, an inverter is required between the ac power source and the dc link in order to enable power transfer to the grid, forming a V2G connection.

### B. Self-Tuning Capability

The power electronic converters used in IPT systems should operate at the resonance frequency of the system in order to achieve the maximum power transfer efficiency. Any deviation from the resonance frequency can dramatically affect the performance of the system. Due to different operating conditions in IPT systems, such as a transmitter and receiver alignment, load characteristics, etc., the characteristics of the system, including resonance frequency, may change. Also, different IPT systems can be designed based on a range of operating resonance frequencies (e.g., 20–85 kHz for inductive EV charging systems). Furthermore, IPT systems can have a variable resonance frequency for different purposes [31]. Therefore, the use of self-tuning controllers that can track and tune the switching operations of the converters with the resonance frequency of the IPT system would be of great interest, as it eliminates the need for manual tuning and can significantly enhance the performance of the system.

The proposed controller (see Fig. 3) synchronizes the switching signals with the resonant current of the IPT system to enable the self-tuning capability. This is achieved by using the resonant current sign signal ( $S_{sgn}$  determined by the differential comparator), and its complement  $\overline{S_{sgn}}$  as clock sources for the entire control circuit. This ensures that the switching operations always occur at the resonant current zero-crossing points, and therefore, the converter is switched at the resonance frequency. This also enables ZCS operations that significantly enhance the performance of the converter and reduce switching stress.

## III. THEORETICAL ANALYSIS

The proposed power controller achieves power transfer control based on resonant current regulation. Therefore, finding an analytical solution for the resonant current in an IPT system would be useful in order to calculate the power transfer level at different energy-injection frequencies.

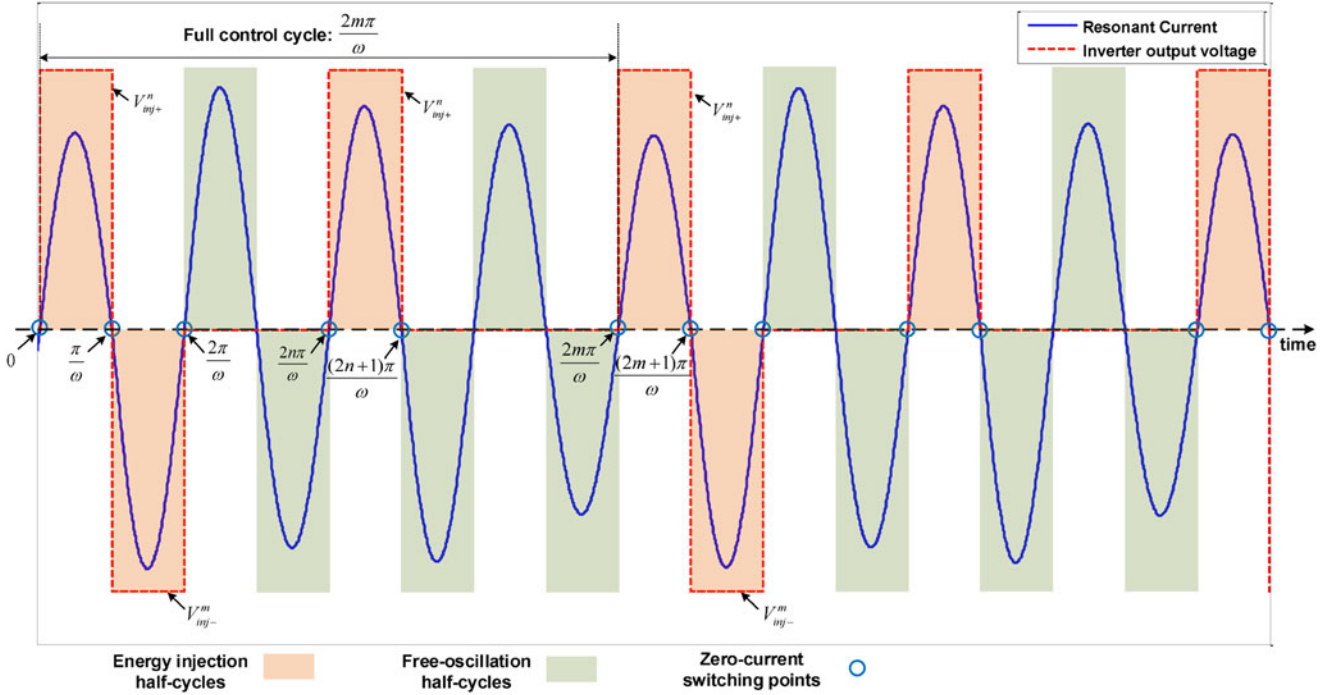


Fig. 4. Resonant current and corresponding switching signals controlled using the proposed controller for power level 2–4 ( $n = 2, m = 4$ ).

#### A. Power Transfer Level

In an  $RLC$  circuit, shown in Fig. 3, the equation for the resonant current can be written as follows:

$$L \frac{di}{dt} + \frac{1}{C} \int i dt + R_{eq} i = V_{inj+}^n(t) + V_{inj-}^m(t) \quad (1)$$

where  $i$  is the resonant current,  $V_{inj+}^n(t)$  and  $V_{inj-}^m(t)$  are output voltage pulses of the converter at energy-injection level  $n-m$  in positive and negative half-cycles, respectively. In Fig. 4,  $V_{inj+}^n(t)$  and  $V_{inj-}^m(t)$  for power level 2–4 ( $n = 2$  and  $m = 4$ ) are conceptually shown. These input functions are periodic with cycles of  $2n\pi/\omega$  and  $2m\pi/\omega$  ( $\omega$  is the frequency of the resonant current), and can be expressed as follows:

$$V_{inj+}^n(t) = \begin{cases} V_t & 0 < t < \frac{\pi}{\omega} \\ 0 & \frac{\pi}{\omega} < t < \frac{2n\pi}{\omega} \end{cases} \quad (2)$$

$$V_{inj-}^m(t) = \begin{cases} -V_t & \frac{\pi}{\omega} < t < \frac{2\pi}{\omega} \\ 0 & 0 < t < \frac{\pi}{\omega}, \frac{2\pi}{\omega} < t < \frac{2m\pi}{\omega} \end{cases} \quad (3)$$

Equation (1) can be solved by applying the superposition law and considering  $V_{inj+}^n(t)$  and  $V_{inj-}^m(t)$  as two separate input functions

$$L \frac{di_1}{dt} + \frac{1}{C} \int i_1 dt + R_{eq} i_1 = V_{inj+}^n(t) \quad (4)$$

$$L \frac{di_2}{dt} + \frac{1}{C} \int i_2 dt + R_{eq} i_2 = V_{inj-}^m(t) \quad (5)$$

where  $i_1$  and  $i_2$  are corresponding solutions due to  $V_{inj+}^n(t)$  and  $V_{inj-}^m(t)$  input functions, respectively. First, the analytical solution for  $i_1$  is found. Since in each half-cycle  $V_{inj+}^n(t)$  is constant,

(4) can be rewritten as follows:

$$\frac{d^2 i_1}{dt^2} + \frac{R_{eq}}{L} \frac{di_1}{dt} + \frac{1}{LC} i_1 = 0. \quad (6)$$

The controller is designed in way that ZCS is obtained. Therefore, the initial conditions would be as follows:

$$i_1(0) = 0, \quad L \frac{di_1}{dt}(0) = V_{inj+}^n(t) - v_c(0) \quad (7)$$

where  $V_{inj+}^n(t)$  is the converter output voltage, and  $v_c(0)$  is the initial capacitor voltage. Therefore, the solution of (6) would be as follows:

$$i_1 = \frac{V_{inj+}^n - v_c(0)}{\omega L} e^{-t/\tau} \sin(\omega t). \quad (8)$$

where  $\omega = \sqrt{\omega_0^2 - 1/\tau^2}$  is the natural resonance frequency,  $\omega_0 = 1/\sqrt{LC}$  is the resonance frequency, and  $\tau = 2L/R_{eq}$  is the damping time constant. Assuming that the system has reached to a steady-state condition,  $v_c(0)$  can be calculated as follows [22]:

$$v_c(0) = -\frac{(1 + \beta)}{1 - \beta^{2n}} \beta^{2n-1} V_t \quad (9)$$

where  $\beta = e^{-\frac{\pi}{\tau\omega}}$ . Using (2), (8), and (9),  $i_1$  can be derived as follows:

$$i_1(t) = \begin{cases} \frac{1 + \beta^{2n-1}}{\omega L(1 - \beta^{2n})} V_t e^{-t/\tau} \sin(\omega t) & 0 < t < \frac{\pi}{\omega} \\ \frac{(1 + \beta)\beta^{2n-1}}{\omega L(1 - \beta^{2n})} V_t e^{-t/\tau} \sin(\omega t) & \frac{\pi}{\omega} < t < \frac{2n\pi}{\omega} \end{cases} \quad (10)$$

Since negative half-cycle energy injection always happens after a positive half-cycle energy injection, the following can be obtained:

$$V_{\text{inj-}}^m(t) = -V_{\text{inj+}}^m\left(t - \frac{\pi}{\omega}\right). \quad (11)$$

Since (4) is linear and time invariant, based on (11), the following is obtained:

$$i_2(t) = -i_1\left(t - \frac{\pi}{\omega}\right)\Big|_{n=m}. \quad (12)$$

In order to eliminate the power levels that will result in a repetitive power level, the proposed controller is designed in a way that  $n \leq m$ . Using (12) and (10),  $i_2$  can be written as follows:

$$i_2(t) = \begin{cases} \frac{(1 + \beta)\beta^{2m-2}}{\omega L(1 - \beta^{2m})} V_t e^{-t/\tau} \sin(\omega t) & 0 < t < \frac{\pi}{\omega} \\ \frac{1 + \beta^{2m-1}}{\omega L(1 - \beta^{2m})\beta} V_t e^{-t/\tau} \sin(\omega t) & \frac{\pi}{\omega} < t < \frac{2m\pi}{\omega} \end{cases}. \quad (13)$$

Applying the superposition principle for differential equations, the final solution for the resonant current can be expressed as follows:

$$i = i_1 + i_2. \quad (14)$$

Using the analytical solution for the resonant current, the transferred power can be obtained as follows:

$$P_{\text{inj}} = \frac{\int_0^{\frac{2m\pi}{\omega}} (V_{\text{inj+}}^n(t) + V_{\text{inj-}}^m(t)) i(t) dt}{2m\pi/\omega}. \quad (15)$$

Considering the fact that in a full cycle ( $0 < t < 2m\pi/\omega$ ) there would be  $m/n$  positive half-cycle energy injections and only one negative half-cycle energy injection, (15) can be rewritten as follows:

$$P_{\text{inj}} = \frac{\sum_{i=1}^{m/n} \int_{2(i-1)\pi/\omega}^{2i\pi/\omega} V_{\text{dc}} i(t) dt + \int_{\pi/\omega}^{2\pi/\omega} -V_{\text{dc}} i(t) dt}{2m\pi/\omega}. \quad (16)$$

Using (10), (13), and (16), the power transfer level can be calculated based on IPT system parameters  $L$ ,  $C$ ,  $R_{\text{eq}}$ , dc-link voltage  $V_{\text{dc}}$ , and power transfer level  $n-m$ . This equation is specifically useful for estimating the output power at different power transfer levels given in Table I.

### B. Voltage Gain of the Converter

Since the proposed controller tunes the output voltage of the converter by switching to different modes of operation, its voltage gain characteristic would be of great interest. The root mean square (rms) output voltage at power transfer level  $n-m$  can be calculated as follows:

$$V_{\text{rms}} = \sqrt{\frac{\int_0^{2m\pi/\omega} V_t^2 dt}{2m\pi/\omega}}. \quad (17)$$

Based on Fig. 4, (17) can be rewritten as

$$V_{\text{rms}} = \sqrt{\frac{\sum_{i=1}^{m/n} \int_{2(i-1)\pi/\omega}^{2i\pi/\omega} V_{\text{dc}}^2 dt + \int_{\pi/\omega}^{2\pi/\omega} V_{\text{dc}}^2 dt}{2m\pi/\omega}}. \quad (18)$$

Equation (18) can be simplified as follows:

$$V_{\text{rms}} = \sqrt{\frac{(m/n + 1) V_{\text{dc}}^2 \pi/\omega}{2m\pi/\omega}} = \sqrt{\frac{n + m}{2nm}} V_{\text{dc}}. \quad (19)$$

Using (19), the voltage gain of the converter can be obtained as follows:

$$G_v = \frac{V_{\text{rms}}}{V_{\text{dc}}} = \sqrt{\frac{n + m}{2nm}} \quad (20)$$

According to (20), the converter using the proposed controller operates as a controlled voltage source for the primary with control parameters  $n$  and  $m$ . In IPT systems (specifically dynamic IPT systems),  $R_{\text{eq}}$  can change due to inherent variations of the system, such as vehicle alignment relative to primary and number of charging vehicles. The controller is designed to regulate the voltage gain with the variations of  $R_{\text{eq}}$  to achieve the desired power transfer level ( $P_{\text{ref}}$ ). For instance, if  $R_{\text{eq}}$  decreases, the output voltage of the converter is reduced ( $n$  and/or  $m$  are increased) to regulate the power level around  $P_{\text{ref}}$ . In other words, lower  $R_{\text{eq}}$  results in lower energy-injection levels (higher  $n$  and/or  $m$ ). At a fixed energy-injection level (no power level regulation), the rms output voltage of the converter is constant, therefore there would be an inverse relationship between power level and  $R_{\text{eq}}$ .

### C. System Response Time

Since an IPT system can be represented with an equivalent  $RLC$  circuit (shown in Fig. 3), the settling time of the system within 2% of the final value can be expressed as follows:

$$T_s \simeq 4\tau = \frac{8L}{R_{\text{eq}}}. \quad (21)$$

Equation (1) shows that there is an inverse relationship between response time of the system and  $R_{\text{eq}}$ . The relationship between power level and different system parameters including  $R_{\text{eq}}$  is presented in (16).

### D. Steady-State Error

As discussed in Section II, the proposed controller operates based on ten discrete power transfer levels presented in Table I. This means that the controller switches between these discrete power levels to minimize the output power error. In Fig. 5, the output power and steady-state error are plotted as a function of reference power. The output power (P.U.) is calculated using (16) at different energy-injection levels, and the relationship between the output power and the reference power (P.U.) is determined based on the design of the controller. Fig. 5 shows that the maximum steady-state error of the system is 22%.

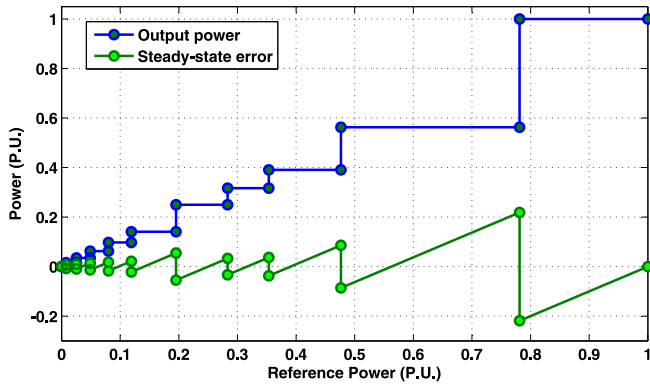


Fig. 5. Output power and steady-state error as a function of reference power.

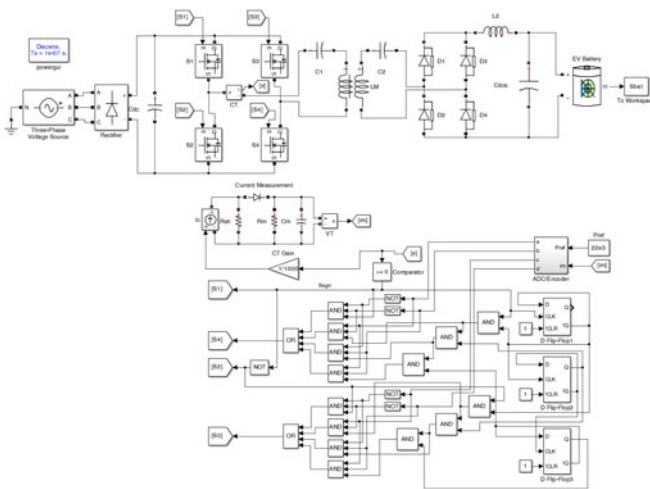


Fig. 6. Case-study IPT system simulation model.

TABLE II  
SPECIFICATIONS OF THE CASE-STUDY IPT SYSTEM

| Parameter                                     | Value       |
|---|-------------|
| Primary and secondary self-inductances        | 172 $\mu$ H |
| Primary and secondary compensation capacitors | 120 nF      |
| Resonance frequency                           | 35 kHz      |
| Grid line voltage                             | 208 V       |
| EV battery voltage                            | 360 V       |
| EV battery capacity                           | 22 kWh      |

#### IV. SIMULATION RESULTS

The proposed controller along with an IPT system is modeled and simulated in MATLAB/Simulink using SimPowerSystem toolbox, and the performance of power transfer regulation is evaluated at different conditions. The simulation model and the specifications of the IPT system are presented in Fig. 6 and Table II, respectively. The IPT system is comprised of a three-phase two-stage ac/dc/ac converter connected to the primary circuit, magnetic couplers, compensation capacitors, and a secondary ac/dc converter that charges an EV battery. The power controller is modeled based on the control circuit presented in

TABLE III  
DISTINCT POWER TRANSFER LEVELS AND CORRESPONDING ENERGY-INJECTION FREQUENCIES FOR POSITIVE AND NEGATIVE HALF-CYCLES

| Power Level $n-m$ | Grid Power (kW) | Grid Current (A) | Battery Charging Current (A) | Battery Charging Power (kW) | Efficiency (%) |
|-------------------|-----------------|------------------|------------------------------|-----------------------------|----------------|
| 1-1               | 33.83           | 112.65           | 92.61                        | 33.34                       | 98.54          |
| 1-2               | 23.28           | 89.56            | 63.28                        | 22.75                       | 97.72          |
| 1-3               | 18.76           | 78.97            | 50.81                        | 18.21                       | 97.07          |
| 1-4               | 16.60           | 73.76            | 45.17                        | 16.06                       | 96.77          |
| 2-2               | 14.51           | 68.33            | 39.38                        | 13.97                       | 96.27          |
| 2-3               | 10.48           | 56.98            | 28.14                        | 9.97                        | 95.17          |
| 2-4               | 8.55            | 50.80            | 22.66                        | 8.04                        | 94.08          |
| 3-3               | 6.65            | 44.38            | 17.04                        | 6.18                        | 92.87          |
| 3-4               | 4.80            | 36.94            | 12.80                        | 4.37                        | 91.01          |
| 4-4               | 3.00            | 28.16            | 7.95                         | 2.63                        | 87.75          |

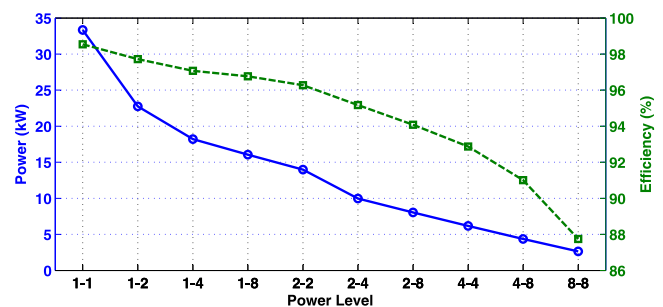


Fig. 7. Power and efficiency of the converter at different power transfer levels calculated based on simulation results.

Fig. 3 using AND, OR, and NOT logic gates, flip-flops, ADC conversion. The voltage comparator is modeled as a “compare to zero” block that acts as a zero-cross detector. The current measurement transformer is modeled as a controlled current source with a 1:1000 conversion ratio. The current measurement signal is converted into a dc signal using a half-wave rectifier, which is then connected to the ADC/Encoder block in order to switch the controller to the appropriate power transfer level. The controller generates the switching signals of the second stage (inverter stage) of the primary converter. The reference power level is determined using (16), based on the energy-injection levels for positive and negative half-cycles ( $n$  and  $m$ ).

The simulations are carried out for all power levels according to Table I, and the results are presented in Table III. The results include grid power and current (rms), battery charging power and current, and the efficiency of the system. Also, the power level and efficiency of the system at different power levels are presented in Fig. 7, which shows that as the power level drops (higher  $n$  and/or  $m$ ), the efficiency of the converter drops. It is due to the fact that at lower power levels, the number of free-oscillation cycles are increased by the controller, in order to reduce energy injection into the IPT system, thereby allowing the resonant current to freely oscillate through the switches of the converter. This, in turn, increases conduction losses in the converter. Fig. 7 also shows that for the first five power levels (levels 1-1, 1-2, 1-4, 2-2, and 2-4), the converter can achieve

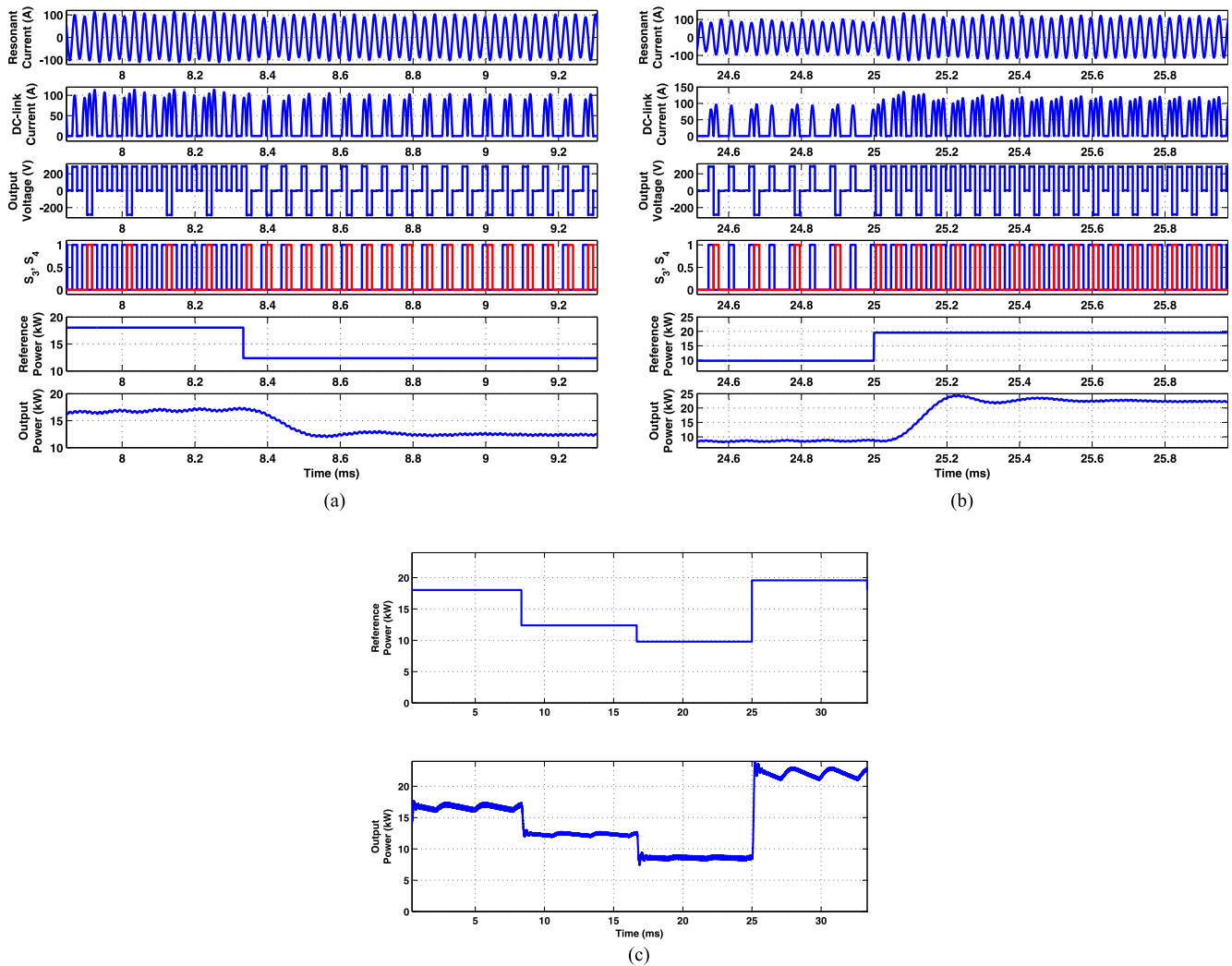


Fig. 8. Simulation results on the case-study IPT system showing resonant current, dc-link current, energy-injection switching signals ( $S_3, S_4$ ), reference power, and output power: (a) transition from level 1–4 (18 kW) to level 2–2 (12 kW); (b) transition from level 2–4 (10 kW) to level 1–2 (20 kW); and (c) transition from level 1–4 (18 kW), level 2–2 (12 kW), level 2–4 (10 kW), to level 1–2 (20 kW).

a minimum efficiency of 96%. Furthermore, the maximum efficiency that is achieved at level 1–1 with 33.83 kW power is 98.54%.

By applying step changes in the reference power level, the performance of the controller is analyzed in tracking the reference power level. In Fig. 8, the simulation results, including resonant current, dc-link current, energy-injection switching signals, reference power, and output power, are presented for different power level transitions. The output power is calculated based on the power delivered to batteries at the secondary circuit. Fig. 8(a) shows the transition from level 1–4 (18 kW) to level 2–2 (12 kW). In Fig. 8(b), transition from level 2–4 (10 kW) to level 1–2 (20 kW) is shown. Also, in Fig. 8(c), transition from level 1–4 (18 kW), level 2–2 (12 kW), level 2–4 (10 kW) to level 1–2 (20 kW) are presented. The results show that using the proposed controller, the output power of the IPT system effectively tracks the reference current (estimated output power) with low discrepancy. The controller effectively changes the energy-injection frequencies in order to conform

to the reference power level. In Fig. 8(a) and (b), it can be seen that the switching operations always occur at the resonant current zero-crossing points, which verifies the self-tuning capability of the controller and ZCS in the converter described in Section II-B.

## V. EXPERIMENTAL RESULTS

In order to validate the effectiveness of the proposed control circuit for controlling the power transfer in the IPT system, experimental test results were carried out on a case-study IPT system. The case study system, shown in Fig. 9, is composed of two circular transmitter and receiver magnetic structures, primary three-phase converter, compensation capacitors, and a battery charger connected to a 12-V battery at the receiver side. The primary converter is a two-stage ac/dc/ac converter whose first stage is a full-bridge three-phase ac/dc converter connected to a 60-Hz variable three-phase source and the second stage is a full-bridge single-phase dc/ac converter that is controlled with

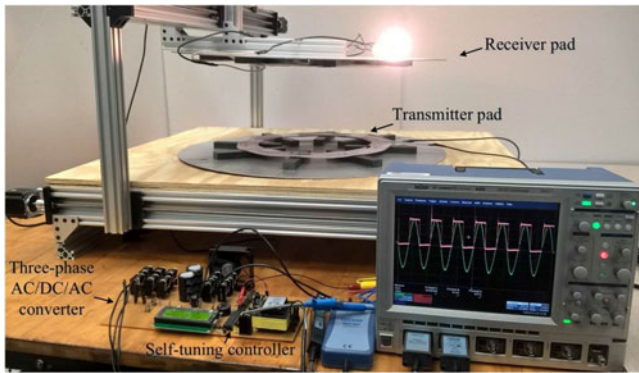


Fig. 9. Experimental setup of the proposed power-frequency controller.

TABLE IV  
SPECIFICATIONS OF THE EXPERIMENTAL IPT SYSTEM

| Parameter               | Components                     | Value            |
|-------------------------|--------------------------------|------------------|
| Pad self-inductance     | 15 turns, 10 AWG Litz wire     | 172 $\mu$ H      |
| Compensation capacitors | Film capacitor, FPG66Y0124J    | 120 nF           |
| Primary supply          | Variable three-phase ac supply | 10 V (LL), 60 Hz |
| Secondary battery       | Lead-acid battery              | 12 V, 86.4 Wh    |

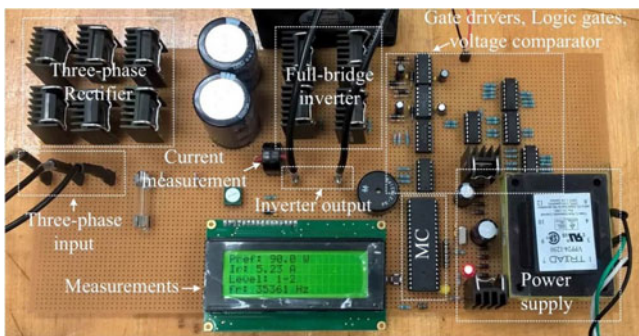


Fig. 10. Experimental setup of the proposed controller and its components.

the proposed power controller. The specifications of the circular power pads, compensation capacitors, primary ac supply, and secondary battery conform to the ones given in Table IV. The resonance frequency of the IPT system is 35 kHz. The proposed control circuit, presented in Fig. 3, is implemented experimentally and is shown in Fig. 10. Also, the circuit components used in building the controller and converter prototype are listed in Table V. The logic gates the differential comparator is used to detect resonant current zero-crossing points. The logic gates and flip-flops are utilized to build the three-stage resonance frequency divider and four-input multiplexers (described in Section II-A). A ten-level ADC along with an encoder are implemented using an Atmel Atmega32 microcontroller.

The performance of the controller is evaluated by applying step changes in the reference power level, which causes changes in the energy-injection frequencies. In Fig. 11(a) and (b), the res-

TABLE V  
LIST OF COMPONENTS USED IN EXPERIMENTAL IMPLEMENTATION OF THE PROPOSED POWER CONTROLLER

| Component                                      | Part Number    |
|--|----------------|
| Switches ( $S_1$ , $S_2$ , $S_3$ , and $S_4$ ) | CREE CMF20120D |
| Gate driver                                    | IR2110         |
| Current transducer                             | PE-51688       |
| Differential comparator                        | TLC374         |
| NOT gate                                       | SN74LS04       |
| AND gate                                       | SN74HC08       |
| OR gate  | M74HC4072      |
| Flip-flop                                      | SN74LS74       |
| ADC, Encoder                                   | Atmel ATmega32 |

onant current, battery charging current, and negative half-cycle energy-injection signals ( $S_3$ ) during the transitions from level 1–8 to level 1–1 and from level 2–1 to level 2–8 are shown. These figures show that the controller can effectively regulate the battery charging current and thereby the power transfer level according to the reference power level. Also, in Fig. 12(a) and (b), the resonant current, primary dc-link current, and energy-injection switching signals ( $S_3$  and  $S_4$ ) for level 1–4 and level 2–2 power are shown. These figures show that the converter achieves ZCS by self-tuning of the switching operations to the resonant current. Experimental results of the converter output voltage (switch node voltage) and the resonant current at power level 2–4 are presented in Fig. 13. This figure shows that the converter achieves ZCS operations. In free-oscillation modes, the output voltage equals to the voltage drop across two conducting switches ( $S_1$  and  $S_3$ , or  $S_2$  and  $S_4$ ) consisting of a body diode and a forward biased switch. In energy-injection modes, the output voltage equals to  $V_{dc}$  or  $-V_{dc}$ , incorporating the voltage drops across two conducting switches ( $S_1$  and  $S_4$ , or  $S_2$  and  $S_3$ ).

#### A. Efficiency Analysis

The power transfer at different levels with a maximum of 500 W calculated based on the experimental measurements on the case-study IPT system setup and theoretical calculations is presented in Fig. 14(a). This figure shows that the experimental measurements of power transfer at different power levels conform to the theoretical calculations with a small discrepancy. In Fig. 14(b), experimental efficiency measurements on the IPT system setup using both the proposed power controller and conventional controller at different power transfer levels are presented and compared with the simulation results at high-power levels. The conventional controller is designed based on the firing angle control with respect to resonant current zero-crossing points in order to regulate the resonant current and the power transfer rate. The figure shows that for low power rates (500 W), the converter can achieve a power transfer efficiency of 96% using both control methods. However, as the power level is decreased, the proposed power control method performs better and achieves higher efficiencies. This is due to the fact that the proposed power control method benefits from soft-switching operations. Also, based on Fig. 14(b), it can be seen that the converter achieves efficiencies above 98% at high-power levels

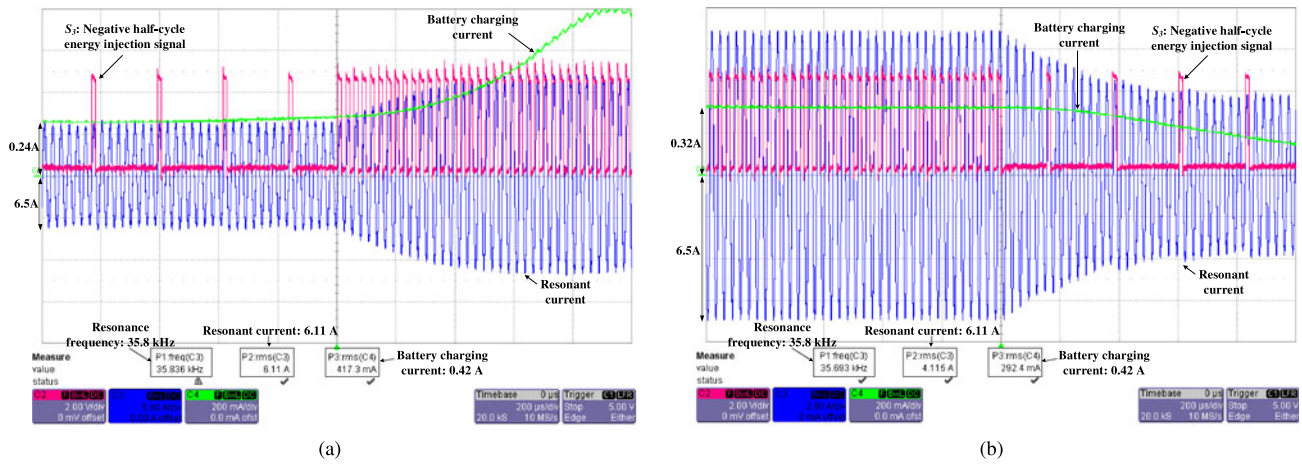


Fig. 11. Experimental results on the IPT setup showing the resonant current, battery charging current, and negative half-cycle switching signal ( $S_3$ ): (a) transition from level 1–8 to level 1–1; and (b) transition from level 1–1 to level 1–8.

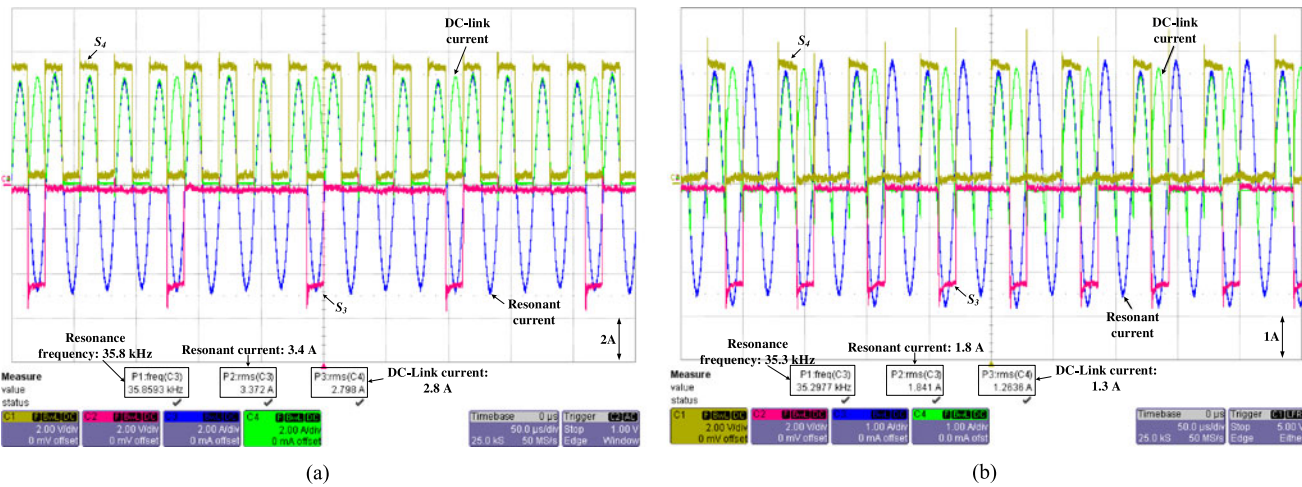


Fig. 12. Experimental results on the IPT setup showing the resonant current, primary dc-link current, and energy-injection switching signals ( $S_3$  and  $S_4$ ): (a) level 1–4 power transfer; and (b) level 2–2 power transfer.

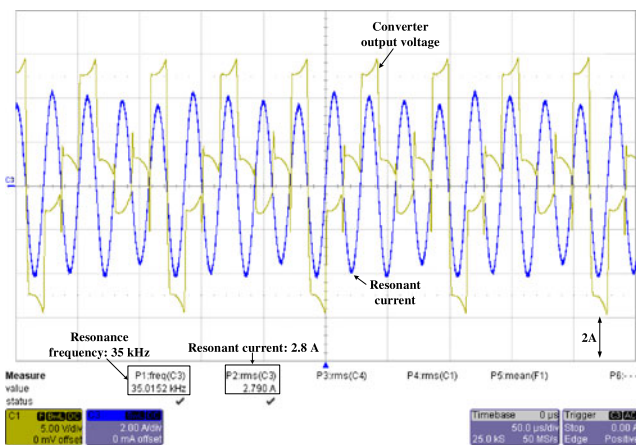


Fig. 13. Output voltage of the dc/ac converter and resonant current at power level 2–4.

(at level 1–1), which is only about 2% higher than efficiency measurements at low-power level.

In Fig. 14(b), experimental efficiency measurements on the IPT systems setup using both the proposed power controller and conventional controllers at different power transfer levels are presented and are compared with the simulation results at high-power levels. The conventional controller is designed based on the switching firing angle control with respect to the resonant current zero-crossing points to regulate the resonant current and the power transfer rate. The figure shows that for low power rates (500 W), using both control methods, the converter can achieve a power transfer efficiency of 96%. But as the power level is decreased, the proposed power control method performs better and achieves higher efficiencies. This is due to the fact that the proposed power control method benefits from soft-switching operations. Also, based on Fig. 14(b), it can be seen that the converter achieves efficiencies above 98% at high-power levels

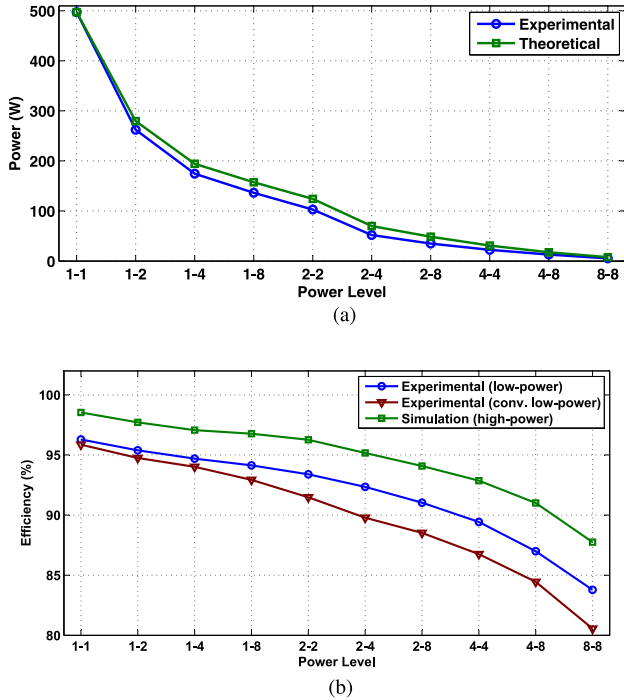


Fig. 14. Experimental results on the case-study IPT system at different power levels: (a) output power obtained based on experimental measurements and theoretical calculations; and (b) converter efficiency obtained based on experimental measurements and simulation results.

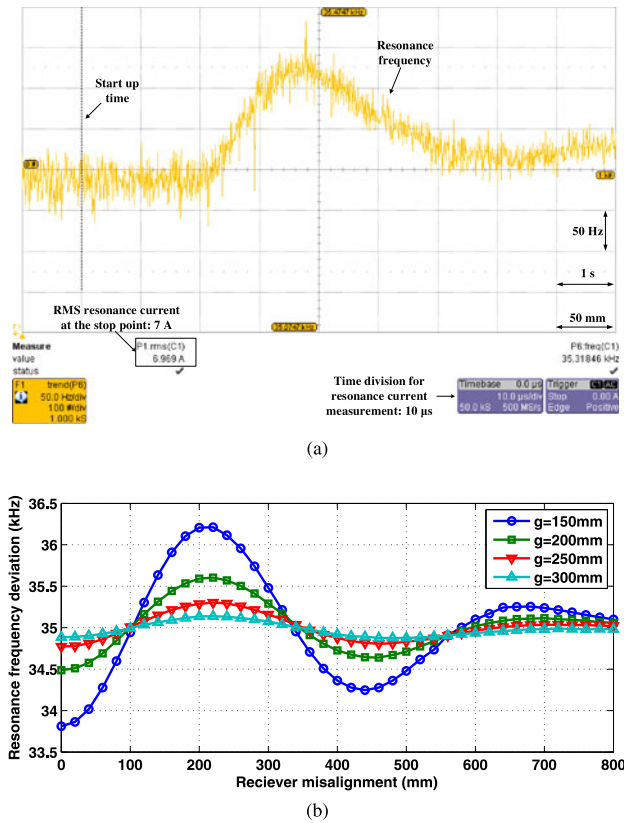


Fig. 15. Experimental frequency measurement results: (a) dynamic resonance frequency variations during the horizontal movement of the secondary pad at 50 mm/s speed and 200 mm air gap; and (b) resonance frequency measurements with variations in distance between the transmitter and receiver power pads (g: air gap).

(at level 1–1), which is only about 2% higher than efficiency measurements at low-power level.

### B. Resonance Frequency Tracking Capability Analysis

In order to verify the resonance frequency tracking capability of the controller, the case-study IPT system is investigated under different transmitter and receiver pad alignments (vertical and horizontal). Any change in the pad alignment will lead to a change in the characteristics of system, including the resonance frequency. The alignment of the IPT system is controlled using a multiaxis alignment system (shown in Fig. 9). The resonance frequency measurements are carried out with different vertical and horizontal alignments and are presented in Fig. 15. Fig. 15(a) shows the resonance frequency of the IPT system as it dynamically changes when the secondary pad moves horizontally at 200 mm air gap and 50 mm/s speed. This figure shows that the power controller effectively tracks the resonance frequency of the system in dynamically varying conditions. Also, Fig 15(b) shows the steady-state resonance frequency at different horizontal and vertical displacements, which is captured experimentally using the IPT system setup. The results also show that the resonance frequency of the system can deviate by 3.5% due to horizontal misalignments. It is important to note that in the alignment experiment presented above, the vehicle chassis, which may impact the characteristics of the IPT system, is not considered.

## VI. CONCLUSION

This paper proposed a self-tuning controller to effectively control the power transfer level in IPT systems, which uses different predefined energy-injection levels to maintain user-defined power transfer levels. The controller’s self-tuning functionality renders it suitable for dynamic IPT applications where the resonance frequency and the load might vary. The proposed controller can also significantly improve the efficiency and reduce the EMI by enabling soft-switching operations in its full-bridge power converter. The controller is further designed using a simplified digital circuit that can lower costs by eliminating the need for availing more expensive solutions, such as digital signal processing and field programmable gate array. Moreover, it is expected to be operable at high operating frequencies. These salient features of the controller, including low cost and high efficiency, therefore, make it a powerful alternative that can be applied to a wide variety of IPT systems.

## REFERENCES

- [1] P. Li and R. Bashirullah, “A wireless power interface for rechargeable battery operated medical implants,” *IEEE Trans. Circuits Syst. II, Exp. Briefs*, vol. 54, no. 10, pp. 912–916, Oct. 2007.
- [2] J. de Boeij, E. A. Lomonova, and A. J. A. Vandenput, “Optimization of contactless planar actuator with manipulator,” *IEEE Trans. Magn.*, vol. 44, no. 6, pp. 1118–1121, Jun. 2008.
- [3] G. A. Covic and J. T. Boys, “Modern trends in inductive power transfer for transportation applications,” *IEEE J. Emerg. Sel. Topics Power Electron.*, vol. 1, no. 1, pp. 28–41, Mar. 2013.
- [4] S. H. Lee, B. S. Lee, and J. H. Lee, “A new design methodology for a 300-kw, low flux density, large air gap, online wireless power transfer system,” *IEEE Trans. Ind. Appl.*, vol. 52, no. 5, pp. 4234–4242, Sep. 2016.

- [5] M. Etemadrezaei and S. M. Lukic, "Multilayer tubular conductor for high Q-factor wireless power transfer system resonators," *IEEE Trans. Ind. Appl.*, vol. 52, no. 5, pp. 4170–4178, Sep. 2016.
- [6] C. Park, S. Lee, G. H. Cho, S. Y. Choi, and C. T. Rim, "Two-dimensional inductive power transfer system for mobile robots using evenly displaced multiple pickups," *IEEE Trans. Ind. Appl.*, vol. 50, no. 1, pp. 558–565, Jan. 2014.
- [7] G. Buja, C. T. Rim, and C. C. Mi, "Dynamic charging of electric vehicles by wireless power transfer," *IEEE Trans. Ind. Electron.*, vol. 63, no. 10, pp. 6530–6532, Oct. 2016.
- [8] U. K. Madawala and D. J. Thrimawithana, "A bidirectional inductive power interface for electric vehicles in V2G systems," *IEEE Trans. Ind. Electron.*, vol. 58, no. 10, pp. 4789–4796, Oct. 2011.
- [9] M. J. E. Alam, K. M. Muttaqi, and D. Sutanto, "A controllable local peak-shaving strategy for effective utilization of PEV battery capacity for distribution network support," *IEEE Trans. Ind. Appl.*, vol. 51, no. 3, pp. 2030–2037, May 2015.
- [10] J. A. Suul, S. D'Arco, and G. Guidi, "Virtual synchronous machine-based control of a single-phase bi-directional battery charger for providing vehicle-to-grid services," *IEEE Trans. Ind. Appl.*, vol. 52, no. 4, pp. 3234–3244, Jul. 2016.
- [11] J. M. Miller, O. C. Onar, and M. Chinthavali, "Primary-side power flow control of wireless power transfer for electric vehicle charging," *IEEE J. Emerg. Sel. Topics Power Electron.*, vol. 3, no. 1, pp. 147–162, Mar. 2015.
- [12] P. Si, A. P. Hu, S. Malpas, and D. Budgett, "A frequency control method for regulating wireless power to implantable devices," *IEEE Trans. Biomed. Circuits Syst.*, vol. 2, no. 1, pp. 22–29, Mar. 2008.
- [13] U. K. Madawala, M. Neath, and D. J. Thrimawithana, "A power-frequency controller for bidirectional inductive power transfer systems," *IEEE Trans. Ind. Electron.*, vol. 60, no. 1, pp. 310–317, Jan. 2013.
- [14] Z. U. Zahid *et al.*, "Modeling and control of series-series compensated inductive power transfer system," *IEEE J. Emerg. Sel. Topics Power Electron.*, vol. 3, no. 1, pp. 111–123, Mar. 2015.
- [15] S. Aldhafer, P. C. K. Luk, A. Bati, and J. F. Whidborne, "Wireless power transfer using class E inverter with saturable DC-feed inductor," *IEEE Trans. Ind. Appl.*, vol. 50, no. 4, pp. 2710–2718, Jul. 2014.
- [16] A. Berger, M. Agostinelli, S. Vesti, J. A. Oliver, J. A. Cobos, and M. Huemer, "A wireless charging system applying phase-shift and amplitude control to maximize efficiency and extractable power," *IEEE Trans. Power Electron.*, vol. 30, no. 11, pp. 6338–6348, Nov. 2015.
- [17] J. T. Matysik, "The current and voltage phase shift regulation in resonant converters with integration control," *IEEE Trans. Ind. Electron.*, vol. 54, no. 2, pp. 1240–1242, Apr. 2007.
- [18] A. Namadmalan, "Self-oscillating tuning loops for series resonant inductive power transfer systems," *IEEE Trans. Power Electron.*, vol. 31, no. 10, pp. 7320–7327, Oct. 2016.
- [19] Z. H. Wang, Y. P. Li, Y. Sun, C. S. Tang, and X. Lv, "Load detection model of voltage-fed inductive power transfer system," *IEEE Trans. Power Electron.*, vol. 28, no. 11, pp. 5233–5243, Nov. 2013.
- [20] F. F. A. van der Pijl, M. Castilla, and P. Bauer, "Adaptive sliding-mode control for a multiple-user inductive power transfer system without need for communication," *IEEE Trans. Ind. Electron.*, vol. 60, no. 1, pp. 271–279, Jan. 2013.
- [21] L. G. G. de Vicuna, M. Castilla, J. Miret, J. Matas, and J. M. Guerrero, "Sliding-mode control for a single-phase AC/AC quantum resonant converter," *IEEE Trans. Ind. Electron.*, vol. 56, no. 9, pp. 3496–3504, Sep. 2009.
- [22] M. Moghaddami and A. Sarwat, "Self-tuning variable frequency controller for inductive electric vehicle charging with multiple power levels," *IEEE Trans. Transport. Electr.*, vol. 3, no. 2, pp. 488–495, Jun. 2017.
- [23] A. Namadmalan and J. S. Moghani, "Tunable self-oscillating switching technique for current source induction heating systems," *IEEE Trans. Ind. Electron.*, vol. 61, no. 5, pp. 2556–2563, May 2014.
- [24] S. M. Tayebi and I. Batarseh, "Analysis and optimization of variable-frequency soft-switching peak current mode control techniques for microinverters," *IEEE Trans. Power Electron.*, vol. 33, no. 2, pp. 1644–1653, Feb. 2018.
- [25] H. L. Li, A. P. Hu, and G. A. Covic, "Primary current generation for a contactless power transfer system using free oscillation and energy injection control," *J. Power Electron.*, vol. 11, no. 3, pp. 256–263, 2011.
- [26] M. Moghaddami, A. Anzalchi, and A. I. Sarwat, "Single-stage three-phase AC-AC matrix converter for inductive power transfer systems," *IEEE Trans. Ind. Electron.*, vol. 63, no. 10, pp. 6613–6622, Oct. 2016.
- [27] H. L. Li, A. P. Hu, and G. A. Covic, "A direct AC-AC converter for inductive power-transfer systems," *IEEE Trans. Power Electron.*, vol. 27, no. 2, pp. 661–668, Feb. 2012.
- [28] J. Y. Lee and B. M. Han, "A bidirectional wireless power transfer EV charger using self-resonant PWM," *IEEE Trans. Power Electron.*, vol. 30, no. 4, pp. 1784–1787, Apr. 2015.
- [29] J. I. Rodriguez and S. B. Leeb, "A multilevel inverter topology for inductively coupled power transfer," *IEEE Trans. Power Electron.*, vol. 21, no. 6, pp. 1607–1617, Nov. 2006.
- [30] M. Moghaddami, A. Sundararajan, and A. I. Sarwat, "A self-tuning variable frequency control for multi-level contactless electric vehicle charger," in *Proc. 2016 IEEE Int. Conf. Power Electron., Drives, Energy Syst.*, Dec. 2016, pp. 1–5.
- [31] Z. Zhang, K. T. Chau, C. Qiu, and C. Liu, "Energy encryption for wireless power transfer," *IEEE Trans. Power Electron.*, vol. 30, no. 9, pp. 5237–5246, Sep. 2015.



**Masood Moghaddami** (S'15) received the B.S. degree from the Amirkabir University of Technology, Tehran, Iran, in 2009, and the M.S. degree from the Iran University of Science and Technology, Tehran, in 2012, both in electrical engineering. He is currently working toward the Ph.D. degree in electrical engineering with the Department of Electrical and Computer Engineering, Florida International University, Miami, FL, USA.

His research interests include electromagnetics, power electronics, digital control, and renewable energy systems.



**Aditya Sundararajan** (S'14) received the B.E. degree in computer science and engineering from the Sri Sivasubramaniya Nadar College of Engineering, Chennai, India, in 2013, and the M.S. degree in computer engineering from Florida International University, Miami, FL, USA, in 2014, where he is currently working toward the Ph.D. degree in electrical engineering with the Department of Electrical and Computer Engineering.

His areas of research interest include high-penetration grid-tied distributed photovoltaic big data

analytics for operational visibility and control at subsecond speeds, smart grid cyber-physical systems, security of wearable biometric systems, and proactive solutions against cyber-attacks for ensuring real-time situation awareness and better common operating picture.



**Arif I. Sarwat** (M'08–SM'16) received the M.S. degree in electrical and computer engineering from the University of Florida, Gainesville, FL, USA, and the Ph.D. degree in electrical engineering from the University of South Florida, Tampa, FL, in 2010.

He worked in the industry (SIEMENS) for nine years executing many critical projects. Before joining Florida International University, Miami, FL, as an Assistant Professor, he was an Assistant Professor of electrical engineering at the University at Buffalo, State University of New York, Buffalo, NY, USA. His

significant work in energy storage, microgrid, and demand-side management is demonstrated with Sustainable Electric Energy Delivery Systems, FL. His research interests include smart grids, high-penetration renewable systems, power system reliability, large-scale distributed generation integration, large-scale data analysis, cyber security, and vehicular technology.